scientific reports

OPEN

Structure characteristics and combustion kinetics of the co-pyrolytic char of rice straw and coal gangue

Chunyan Xu[1,3], Chengjia Luo[1], Jun Du[1], Lang Liu[1,2✉], Jingjing Wang[1], Chenhong Yuan[1] & Junjiang Guo[4]

Co-combustion is a technology that enables the simultaneous and efficient utilization of biomass and coal gangue (CG). Nevertheless, the factors that affect the combustibility of co-pyrolytic char, which represents the rate-determining step of the entire co-combustion process, remain unclear. This study investigates the impact of the physicochemical properties of co-pyrolytic char, including pore structure, carbon structure, and alkali metals, on the combustion characteristics. The TGA analysis indicates that the ignition and burnout temperatures of the co-pyrolytic char increase as the CG mixing ratio increases, resulting in a prolonged combustion. This is due to the fact that the carbon structure of the co-pyrolytic char becomes increasingly aromatic, accompanied by a reduction in aliphatic hydrocarbons and oxygen-containing groups as the CG mixing ratio increases. Furthermore, the high ash content of the CG is another significant factor contributing to the observed reduction in combustibility. The reaction between mullite, quartz in CG, and alkali metals in biomass results in the formation of aluminosilicate, which reduces the catalytic ability of alkali metals. Furthermore, the char combustion kinetics are analyzed by the KAS method, and the results indicate that the introduction of CG increases the activation energy of the entire char combustion process. The activation energy of the 80RS20CG is within the range of 102.22–164.99 kJ/mol, while the RS char is within the range of 89.87–144.67 kJ/mol.

Keywords Coal gangue, Co-pyrolytic char, Char characteristics, Combustion kinetics

In light of the dearth of fossil fuels and the imminent challenge of environmental contamination, it is imperative to investigate and develop clean and sustainable alternative sources of energy. Biomass resources are regarded as a prospective clean energy alternative to traditional fossil energy sources, given their abundance, renewability, storability and carbon neutrality[1–3]. Moreover, as a significant agricultural nation, China produces approximately 7.4 million tons of straw biomass annually[4]. The utilization of straw biomass has the potential to offer significant environmental and economic benefits. Thermal conversion technologies, such as pyrolysis, gasification, and combustion, are highly efficient methods for converting biomass into high-value fuel and/or electricity. In these processes, combustion accounts for approximately 97%[5–8]. Nevertheless, biomass typically contains a significant amount of alkali metals, which could result in a number of ash-related issues, such as ash melting, agglomeration, and corrosion, and thus reducing combustion efficiency[9–11]. Meanwhile, coal gangue (CG) is a by-product of the coal mining process[12], and our previous research has demonstrated that the combination of mullite and quartz in CG can react with the alkali metals present in biomass during the combustion to form aluminosilicate with a high melting point[13], helping to alleviate ash issues.

In addition, CG is a low calorific mixture composed of various minerals that is commonly used as a fuel for power generation, but is difficult to ignite and unstable in combustion. While biomass has a high volatile matter content, low ash content, and low ignition temperature[14,15], making it favorable for improving the combustibility of CG[16]. Bi et al.[17] demonstrated that the addition of peanut shells can enhance the combustibility of CG

[1]School of Materials and Environment, Guangxi Minzu University, Nanning 530006, Guangxi, China. [2]Guangxi Key Laboratory of Advanced Structural Materials and Carbon Neutrality, Nanning 530006, Guangxi, China. [3]Guangxi Colleges and Universities Key Laboratory of Environmental-Friendly Materials and Ecological Remediation, Nanning 530006, Guangxi, China. [4]Chemical Engineering Institute, Guizhou Institute of Technology, Guiyang 550003, Guizhou, China. ✉email: l.liu@gxmzu.edu.cn

and increase gas generation during co-combustion. Zhang et al.[18] found that the inclusion of pine sawdust has a positive impact on CG combustion. Bi et al.[19] investigated the co-combustion kinetics of CG and peanut shell by the artificial neural network method. Their findings indicated the activation energy of the co-combustion of CG and peanut shell was significantly lower than that of CG combustion alone. Li et al.[20] demonstrated that the volatile matter precipitated from polypropylene can significantly reduce the activation energy during the initial stage of co-combustion of CG and polypropylene. In conclusion, co-combustion is expected to alleviate the ash problem caused by alkali metals in biomass[13] and enhance the combustion efficiency[21–24], thereby optimizing the utilization of both solid wastes.

Nevertheless, the majority of current studies focus on the kinetics, ash issues and gas generation during the co-combustion, with few scholars paying attention to the combustion characteristics of the co-pyrolytic char, which is the rate-determining step of the entire co-combustion process[25,26]. The combustibility of the co-pyrolytic char is directly correlated with its physicochemical properties, including pore structure, carbon structure and inorganic minerals. Tilghman et al.[27] demonstrated that alterations in the carbon structure of biochar result in changes in its gasification and combustion reactivity. Tong et al.[28] confirmed that the chemical structure is a primary determinant of the biochar activity. Zou et al.[26] demonstrated that the combustion of the biochar is related to the number of the aromatic rings. Meanwhile, the alkali metals present in biomass have the potential to enhance the combustion activity of the biochar[29]. In summary, the char combustion characteristic is directly related to its physicochemical properties, including pore structure, carbon structure and the presence of alkali metals. Moreover, studies have indicated that the minerals present in CG can facilitate the formation of carbon during the biomass pyrolysis[30], resulting in the generation of char with a developed pore structure and stable aliphatic chain structure[31]. Nevertheless, the precise mechanism by which the introduction of CG affects the physicochemical properties of co-pyrolytic char, and the relationship between these physicochemical properties and the combustibility remain unclear.

The objective of this study is to investigate the physicochemical properties of co-pyrolytic char produced with varying biomass and CG mixing ratios, to characterize its combustion behavior, and to examine the influence of the physicochemical properties on the combustion kinetics. The results will provide valuable insights into the interaction between biomass and CG during co-combustion process.

Material and methods

Raw materials

The CG used in this study was sourced from a coal mine in southwestern China, while the rice straw was obtained from rural areas in southern China. Both samples were ground and sieved into particles with a diameter of less than 74 μm, and subsequently air-dried in an oven at 105 °C for 12 h. The proximate, ultimate and heating value analysis of the CG and RS are shown in Table 1. The fixed carbon content in RS and CG is comparable, as evidenced by the proximate analysis. While RS exhibits a markedly higher volatile matter content and a significantly lower ash content than CG. The inorganic mineral compositions in RS and CG are presented in Table 2. It shows that CG mainly contains 52.89% SiO_2, 22.32% Al_2O_3, and 10.12% Fe_2O_3, while RS mainly contains 44.16% SiO_2 and 18.89% K_2O.

Co-pyrolysis experiment

Six feedstocks were obtained by mixing RS and CG in the mass ratios of 100:0, 80:20, 60:40, 40:60, 20:80 and 0:100, respectively. In the co-pyrolysis experiment, 5 g of the feedstocks was spread in an Al_2O_3 crucible and heated up to 500 °C in a tube furnace at a rate of 20 °C/min and held for 30 min under an N_2 atmosphere with a purity of 99.9% by mole. The generated gas was extracted from the tube furnace with N_2 and condensed in two scrubbers immersed in a water bath to collect the generated tar, which was then weighed. The residual char samples were collected and weighed after the furnace had cooled down under an N_2 atmosphere, and named

	Sample	
Properties	**RS**	**CG**
Proximate analysis, ad (wt.%)		
Fixed carbon	15.22	16.23
Volatile matter	78.64	9.61
Ash	6.14	74.16
Ultimate analysis, ad (wt.%)		
C	44.02	17.49
H	4.83	1.18
N	1.72	0.40
O[b]	43.01	4.49
S	0.28	2.28
H/C	1.32	0.81
O/C	0.73	0.19
HHV (MJ/kg)	16.45	5.69

Table 1. Proximate and ultimate analysis and heating value of RS and CG used in this study.

	Sample	
Composition (%)	RS	CG
SiO_2	44.16	52.89
Al_2O_3	3.16	22.32
Fe_2O_3	0.61	10.12
CaO	7.62	3.86
Cl	6.35	0.12
K_2O	18.89	3.12
SO_3	3.89	2.56
Na_2O	3.53	2.32
MgO	6.88	1.72
P_2O_5	2.81	0.48
MnO	1.72	0.21

Table 2. Inorganic minerals composition analysis in ash of CG and RS.

according to the ratio of RS to CG in the feedstocks: RS char, 80RS20CG, 60RS40CG, 40RS60CG, 20RS80CG, and CG char. The schematic diagram of the co-pyrolysis experimental setup is shown in Fig. 1, and all experiments were repeated three times to obtain an average and minimize errors.

Physicochemical characteristics of co-pyrolytic char samples

Various analytical techniques and instruments were used to determine the physicochemical properties of the co-pyrolytic char samples. The pore structure parameters of the co-pyrolytic char samples were determined using an N_2 adsorption technique in a BET apparatus (Micromeritics ASAP 2420). The microstructures were observed using a SEM (ZEISS EVO 18). The organic functional groups were characterized using a FTIR spectrometer (NicoletiS50, Thermofisher Scientific). The carbon structures were analyzed using a Raman spectrometer (Thermo Fischer DXR), and the mineral compositions were determined using XRD (Ultima IV).

Combustion characteristics of the co-pyrolytic char

The combustion experiment of the co-pyrolytic char samples was carried out on a thermogravimetric analyzer (TGA 550, TA). In each experiment, approximately 5 mg char was placed in an Al_2O_3 crucible, which was then heated to 973.15 K at different heating rates in an air atmosphere with a flow rate of 50 mL/min. Meanwhile, the weight losses during the combustion were converted into combustion conversion rates to allow a comparative analysis of the combustion characteristics of the co-pyrolytic char samples, and the combustion conversion was calculated via the Eq. (1):

$$x = \frac{w_0 - w_t}{w_0 - w_\infty} \times 100\% \tag{1}$$

The reaction rate (dx/dt) was calculated by analyzing the combustion conversion rate versus time profiles using Eq. (2).

$$Reaction\ rate = \frac{dx}{dt} \tag{2}$$

where w_0, w_t, and w_∞ denote the initial weight, the weight at the time t and the final weight of the co-pyrolytic char samples during the combustion, respectively.
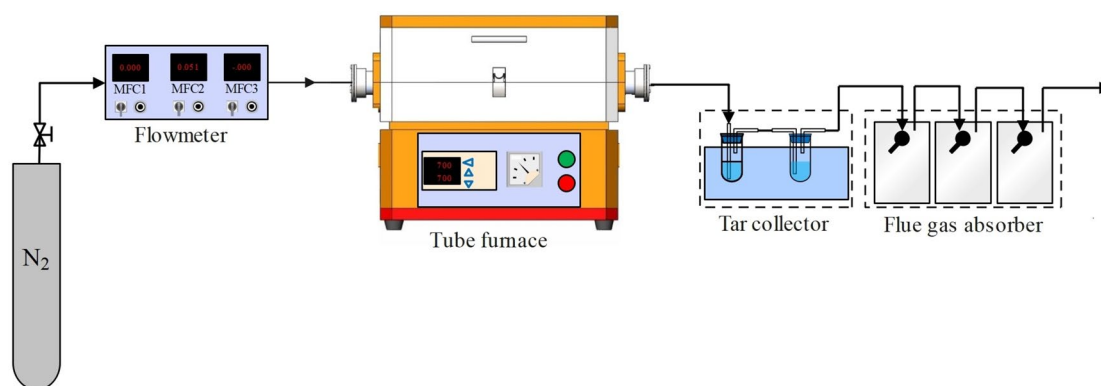

Figure 1. The schematic diagram of the co-pyrolytic experimental setup.

Results and discussion
The mass yields of char, tar and gas during the co-pyrolysis

According to the weight of the generated tar and residual char measured in the pyrolysis experiment, the actual mass yields of char, tar and syngas, named as $Y_{actual\ char}$, $Y_{actual\ tar}$ and $Y_{actual\ gas}$, respectively, can be calculated by Eqs. (3–5). Furthermore, the expected mass yields of char, tar and syngas, named as $Y_{expected\ char}$, $Y_{expected\ tar}$ and $Y_{expected\ gas}$, respectively, based on the assumption that there is no interaction between CG and RS during the pyrolysis are introduced to analyze the influence of CG on RS pyrolysis. The expected mass yields are estimated by Eqs. (6–8).

$$Y_{actual\ char} = W_{char}/W_0 \times 100\% \tag{3}$$

$$Y_{actual\ tar} = W_{tar}/W_0 \times 100\% \tag{4}$$

$$Y_{actual\ gas} = 100\% - Y_{actual\ char} - Y_{actual\ tar} \tag{5}$$

$$Y_{expected\ char} = Y_{RS\ char} \times x_{RS} + Y_{CG\ char} \times x_{CG} \tag{6}$$

$$Y_{expected\ tar} = Y_{RS\ tar} \times x_{RS} + Y_{CG\ tar} \times x_{CG} \tag{7}$$

$$Y_{expected\ gas} = 100\% - Y_{expected\ char} - Y_{expected\ tar} \tag{8}$$

where W_0 is the initial weight of feedstock; W_{char} and W_{tar} are the actual weight of the residual char and generated tar during the pyrolysis, respectively; $Y_{RS\ char}$ and $Y_{RS\ tar}$ are the mass yields of the residual char and tar when RS was pyrolyzed separately, respectively; $Y_{CG\ char}$ and $Y_{CG\ tar}$ are the mass yields of char and tar when CG was pyrolyzed separately, respectively; x_{RS} and x_{RS} represent the mixing ratio of RS and CG in the feedstocks, respectively. The calculated actual mass yields and expected mass yields are given in Fig. 2, and the difference between actual and expected mass yields are presented in Fig. 3. It shows that the values of $Y_{actual\ tar} - Y_{expected\ tar} < 0$, $Y_{actual\ char} - Y_{expected\ char} > 0$ and $Y_{actual\ gas} - Y_{expected\ gas} > 0$ with a CG mixing ratio < 60%. As known, the pyrolysis under N_2 atmosphere mainly involves drying, pyrolysis, and tar cracking, which sequentially undergoes R1 and R2 reactions, and the main products include the residual char, tar and syngas[7]. The volatile matter of the feedstock undergoes cracking to form tar and gas through R1, which is subsequently released, resulting in a decrease in the residual char yield. However, the actual tar yield is lower than the expected tar yield, and the actual char yield is greater than the expected char yield. This is mainly due to the dehydroxylation of kaolinite in CG during pyrolysis delays the residence time, thus accelerating the pyrolysis reaction and increasing the carbon yield[30].

$$Pyrolysis : feedstock \rightarrow char + tar + gas \tag{R1}$$

$$Cracking : tar \rightarrow C + CO + H_2 + CH_4 \ldots \tag{R2}$$
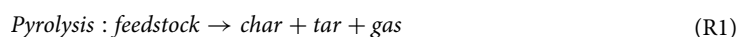
As the CG mixing ratio increase to exceed 60%, the actual char mass yield is greater than the expected char mass yield, which is due to the accumulation of ash in CG hindering the pore structure, and a large number of organic components in RS accumulates on the surface of the ash, inhibiting the release of organic components and subsequent pyrolysis and cracking[30,32].
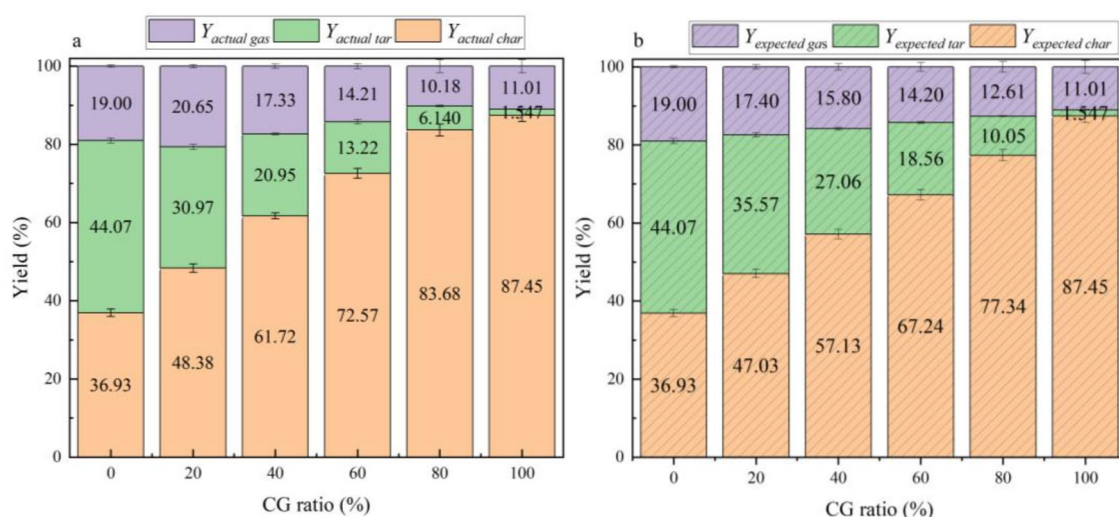

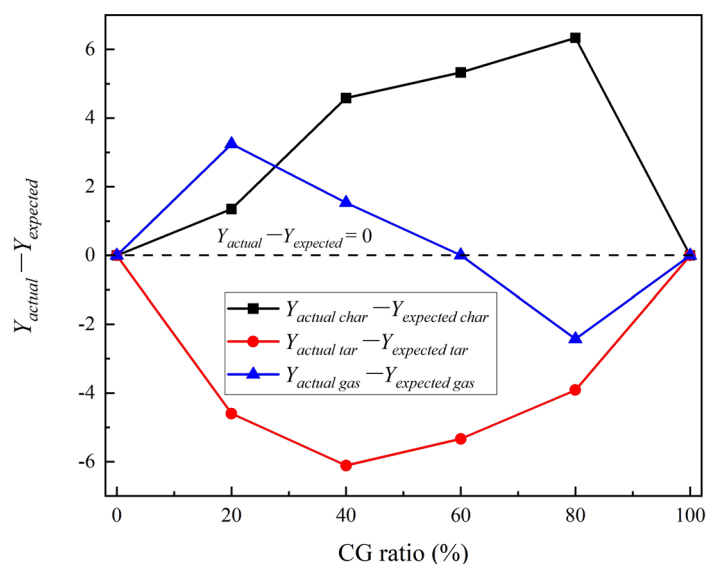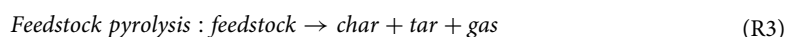**Figure 2.** The actual & expected mass yields of the char, tar and gas during pyrolysis.

Figure 3. Difference between actual and expected mass yields.

$$Feedstock\ pyrolysis : feedstock \rightarrow char + tar + gas \tag{R3}$$

$$Cracking : tar \rightarrow C + CO + H_2 + CH_4 \ldots \tag{R4}$$

Pore structure of the co-pyrolytic char

The pore structural parameters of the co-pyrolytic char samples, including total pore volume and specific surface area, were quantitatively characterized using the N_2 adsorption isotherms method, and the results are shown in Fig. 4. Figure 4 shows that both the total pore volume and the specific surface area increased gradually as the CG mixing ratio increased from 0 to 40%. This is mainly because CG is conducive to catalyzing the pyrolysis of volatile matter in RS into tar, carbon and gas. The formation of tar and syngas can result in the emptying of the pores, while the formation of carbon can act as a skeleton to support these pores, thereby favoring the development of pore structure. As the CG mixing ratio increases from 40 to 100%, the amount of inorganic minerals introduced also increases, which results in the co-pyrolytic char particles becoming more analogous in structure to rock, thereby reducing the pore structure.
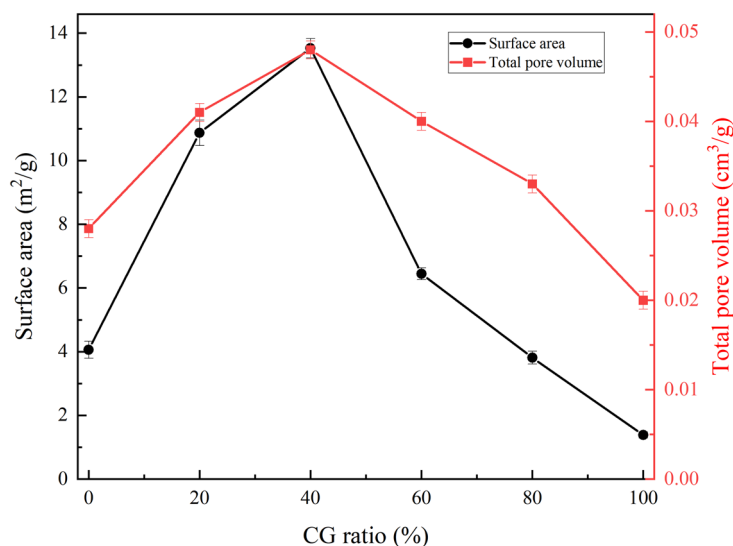

Figure 4. Specific surface area and total pore volume of the co-pyrolytic char samples.

In order to visualize the microstructure of the co-pyrolytic char samples, their micro-morphology was characterized by SEM. The results are shown in Fig. 5, and it shows that broken fiber structures and micro-sphere structures were observed on the surface of the particles in RS char, 80RS20CG and 60RS40CG. However, the number of these structures decreased gradually with an increase in the CG mixing ratio. The primary factors contributing to this phenomenon are that the CG is conducive to the pyrolysis of the cellulose into tar and gas, with the resulting tar undergoing further cracking into carbon and gas[30]. As the CG mixing ratio increases from 40 to 100%, the particles become more regular and smoother. This is due to the introduction of a large number of inorganic minerals by the CG, which results in the surface structure of the co-pyrolytic char particles becoming more similar to the rock structure with fewer dense pores. The rock structure with few dense pores would be expected to increase the resistance to heat and mass transfer, thereby inhibiting the co-pyrolysis of RS and CG.

Chemical structure characteristics of the co-pyrolytic char

The proximate and ultimate analysis of the co-pyrolytic char are presented in Table 3. In comparison to the raw RS, the fixed carbon content in RS char exhibited a notable increase, rising from 15.22 to 55.24%. Conversely, the volatile matter content exhibited a significant decrease, falling from 78.64 to 26.07%. Additionally, the ash content demonstrated an upward trend, increasing from 6.14% to 18.69%. It is well established that the raw RS primarily comprises cellulose, hemicellulose, and lignin. The organic functional groups present in cellulose and hemicellulose undergo a process of breakage and recombination during pyrolysis, resulting in the formation of tar, CO_2, CO, CH_4, and H_2, which in turn leads to a reduction in the volatile matter content[33]. Furthermore, the volatile matter in the RS also undergoes a slow carbon-forming reaction[6,34]. The reduction in the volatile matter content and carbon formation results in an increase in the fixed carbon content in RS char. The results also indicate that as the CG mixing ratio increases from 0 to 100%, the fixed carbon content in the co-pyrolytic char samples gradually decreases from 55.2% to 18.66%, the volatile matter content decreases from 26.07 to 5.22%, and the ash content increases from 18.69 to 76.12%. The contents of C, H, N and O in the char gradually decrease with the increase in CG mixing ratio. The above phenomena are mainly caused by the following two reasons: (1) the volatile matter in RS will break and recombine into tar, CO_2, CO, CH_4 and H_2, and release under such co-pyrolysis condition[2,33]; (2) the addition of CG introduces a large amount of inorganic minerals.

The carbon structures of the different co-pyrolytic char samples were analyzed using the Raman spectroscopy, as shown in Fig. 6a. The Raman spectra of the samples can be roughly designated as a disordered carbon band (D band) at ~ 1380 cm^{-1} and a graphite band (G band) at ~ 1580 cm^{-1}[35,36]. The results indicate that the Raman intensity of co-pyrolytic char exhibits a positive correlation with an increase in the CG mixing ratio increases. The introduction of greater quantities of metal oxides with an elevated of CG mixing ratio has the effect of reducing the light absorptivity, which in turn leads to an increase in the intensity of the Raman peaks. Moreover, the
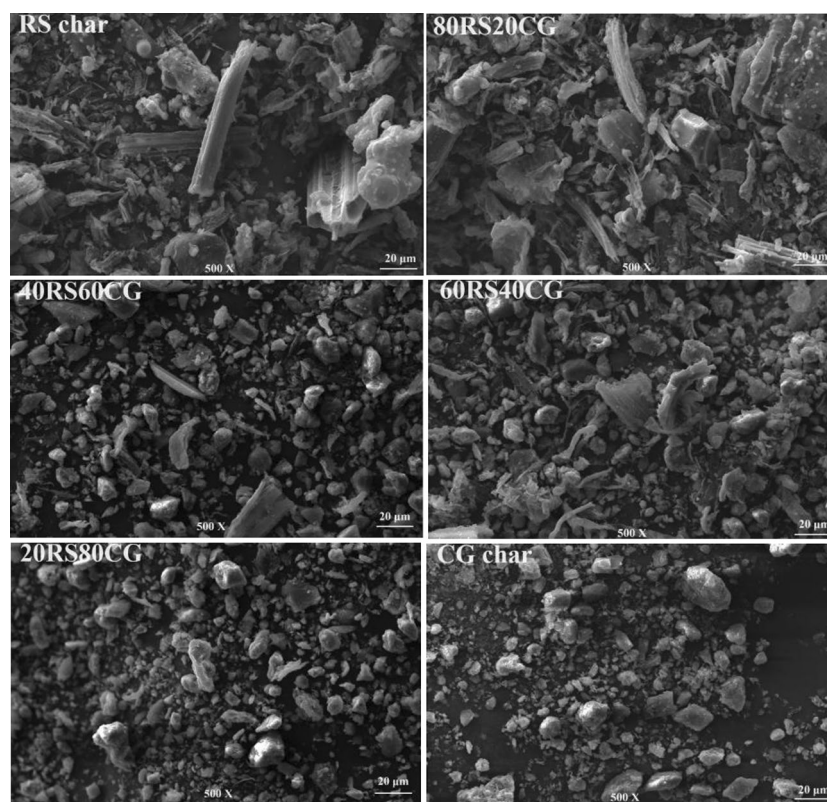

Figure 5. SEM images of the co-pyrolytic char samples.

Properties	Sample					
	RS char	80RS20CG	60RS40CG	40RS60CG	20RS80CG	CG char
Proximate analysis, ad (wt.%)						
Fixed carbon	55.24	43.28	30.58	22.96	19.81	18.66
V olatile matter	26.07	18.22	15.99	10.17	7.61	5.22
Ash	18.69	38.5	53.43	66.87	72.58	76.12
Ultimate analysis, ad (wt.%)						
C	64.42	49.36	36.91	25.56	21.56	19.32
H	2.54	1.99	1.54	1.38	1.27	1.12
N	1.41	0.83	0.57	0.39	0.31	0.24
O^b	12.71	8.31	5.88	3.88	2.28	1.08
S	0.23	1.01	1.67	1.92	2.00	2.12
H/C molar ratio	0.47	0.48	0.50	0.65	0.71	0.70
O/C molar ratio	0.15	0.13	0.12	0.11	0.08	0.04

Table 3. Proximate and ultimate analysis of the co-pyrolytic char samples.
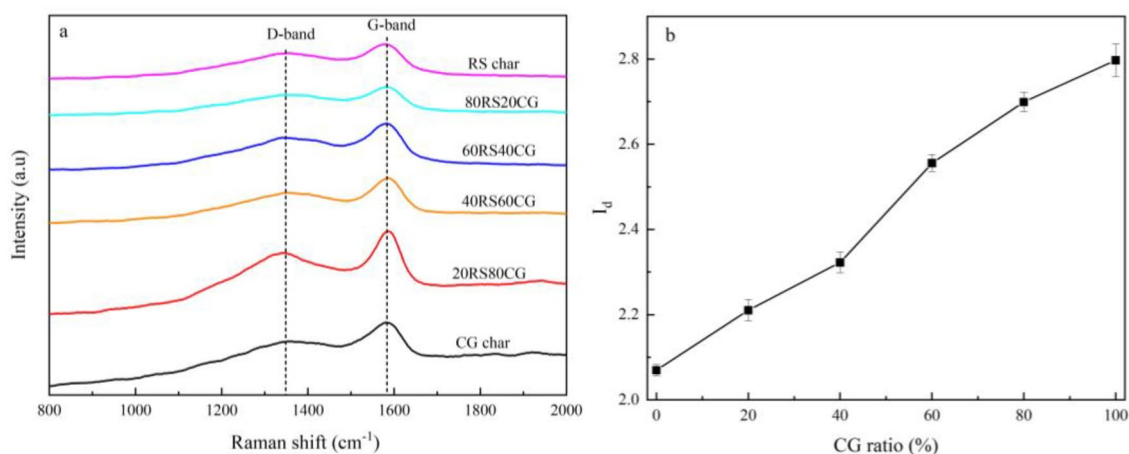

Figure 6. Raman spectra of the co-pyrolytic char samples.

ratio R_d, is a very important parameter to study the carbon structural information in co-pyrolytic char, and is defined as:

$$R_d = \frac{I_d + I_g}{I_g} \qquad (9)$$

where I_d and I_g are referred to the intensities of D-band and G-band, respectively, larger values of R_d indicate more disorder or amorphous carbon in the char[35,36]. The calculated R_d for each co-pyrolytic char sample is shown in Fig. 6b, which demonstrates that the value of R_d increases as the CG mixing ratio decreases. This suggests that the relative content of disordered or amorphous carbon in the co-pyrolytic char increases as the CG mixing ratio increases. This result is consistent with the ultimate analysis of the co-pyrolytic char samples presented in Table 3.

The FTIR spectra were employed to investigate the organic functional groups present in the co-pyrolytic char samples, as shown in Fig. 7. The results demonstrate that the groups present in the co-pyrolytic char samples are primarily comprised of the bending vibration bands of aromatic CH at ~ 780 cm⁻¹ and ~ 1000 cm⁻¹, the aliphatic -CHₙ absorption bands at ~ 1410 cm⁻¹, the aromatic C=C stretching vibration bands at ~ 1605 cm⁻¹, as well as the –OH absorption bands in phenol groups at ~ 3300 cm⁻¹[35,37]. The results also demonstrate that an increase in the CG mixing ratio leads to an enhancement in the peak strength of CH, while the peak strength of –OH, C=C, –CHₙ and C–O bands is reduced. This is attributed to the organic functional groups in CG being predominantly aromatic groups, with the content of other organic functions decreasing as the CG mixing ratio increases. In addition, the inorganic components, such as Fe_2O_3, present in CG can facilitate the cracking of oxygen-containing functional groups in RS. This, in turn, results in a reduction in the content of the C–O and –OH bands[30], thereby rendering the co-pyrolytic char more aromatic.

The inorganic mineral composition and carbon structure of the char samples were determined by XRD, and the results are presented in Fig. 8. The results indicate that the primary minerals present in RS char are quartz and sylvite, while the main minerals in CG char are potassium mica, quartz, alumina and mullite. Whereas, there is no discernible mullite diffraction peak in the XRD curves of 80RS20CG, 60RS40CG, 40RS60CG and
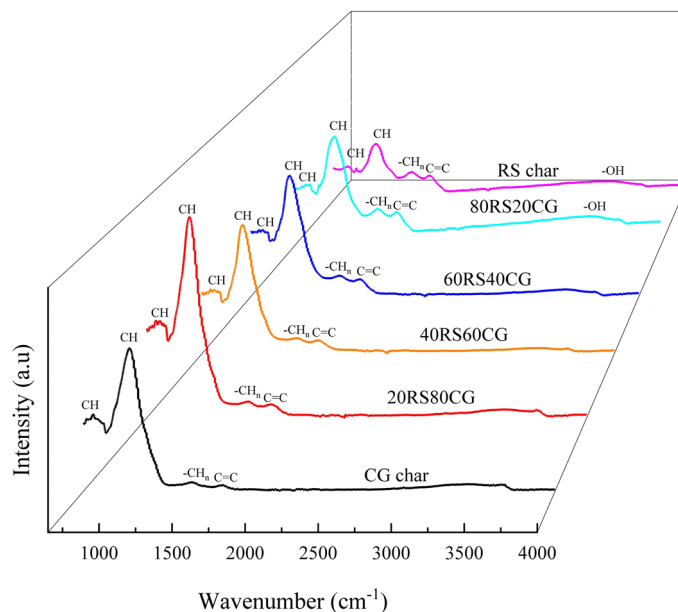
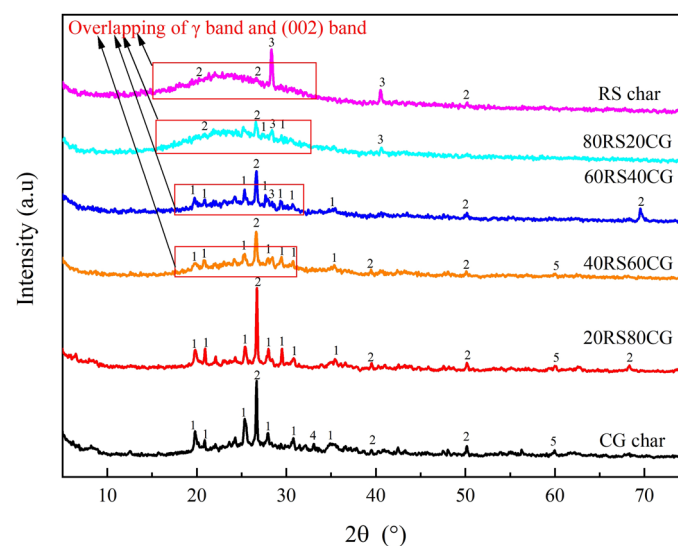**Figure 7.** FTIR spectra of the co-pyrolytic char samples.

Figure 8. XRD patterns of the co-pyrolytic char samples. (1: Potassium mica ($KAl_3Si_3O_{11}$); 2: Quartz (SiO_2); 3: Sylvite (KCl); 4: Mullite ($3Al_2O_3 \cdot 2SiO_2$); 5: Alumina (Al_2O_3)).

20RS80CG. Furthermore, the sylvite diffraction peaks disappear as the CG mixing ratio increase to exceed 60%, indicating that the sylvite should react with mullite and quartz in CG to form potassium mica[13]. Nevertheless, potassium mica is a stable aluminosilicate with minimal catalytic effect on char combustion[38]. The broad bands observed in the range $2\theta \approx 15–26°$ are attributed to the overlap of the γ-bands, which indicates the presence of saturated aliphatic chains[39]. The asymmetric (002) bands observed in the range $2\theta \approx 15–32°$ reflect the degree of parallel orientation of the aromatic structural units[40]. Meanwhile, the background intensity of XRD spectrum is closely connected to the presence of amorphous carbon[41]. It can be observed that the background as well as the intensity of (002) bands and γ-bands gradually decrease in the CG mixing ratio, indicating that the carbon structure in the CG is minimal, which subsequently results in a reduction of amorphous and saturated aliphatic chains in the co-pyrolytic char as the CG mixing ratio increasing.

Combustion characteristics of the co-pyrolytic char

The TGA was employed in this study to investigate the combustion characteristics of the co-pyrolytic char samples. The curves of combustion conversion rate and reaction rate for the co-pyrolytic char samples are presented in Fig. 9. Figure 9 illustrates that the reaction rate curves of the RS char, 80RS20CG, 60RS40CG, 40RS60CG
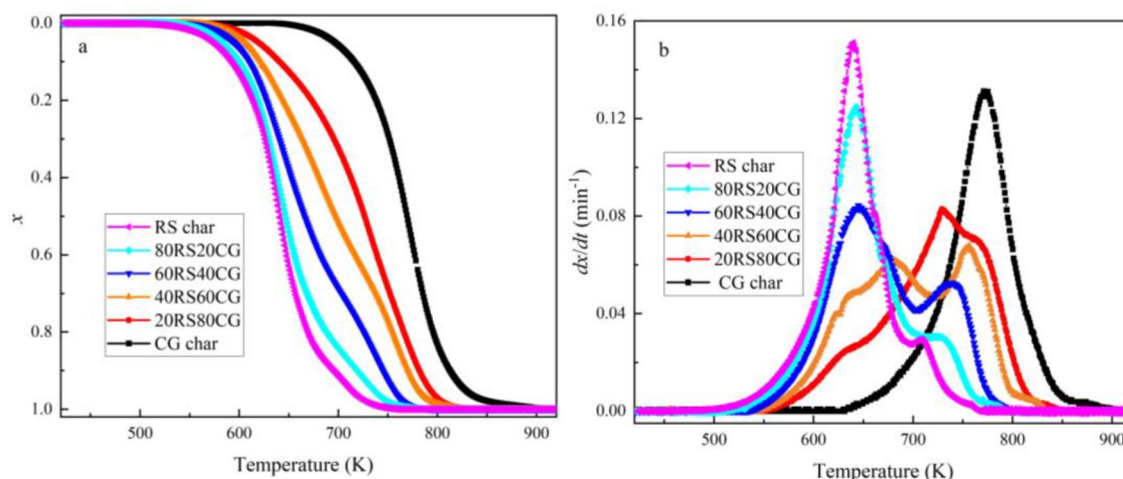
Figure 9. Combustion conversion rate (x) and reaction rate (dx/dt) curves of the co-pyrolytic char samples at 10 K/min under the air atmosphere.

and 20RS80CG exhibit two distinct peaks, suggesting that the combustion process can be divided into two primary stages. As the CG mixing ratio increased, both peaks shift to higher temperatures, accompanied by a decrease in the area of the low-temperature region and an increase in the area of the high-temperature region. As the CG mixing ratio increased to 100%, the CG char combustion primarily occurs between 632 and 912 K, with a single peak in the reaction rate curve observed at the higher temperature (761 K). The primary reason for this discrepancy is that the RS char contains a considerable number of aliphatic rings, oxygen-containing functional groups, and aromatic rings, whereas the functional group in CG char is primarily aromatic rings, as evidenced by the results of the FTIR spectra. In contrast, the oxygen-containing functional groups and aliphatic rings exhibit greater combustion reactivity than the aromatic rings[4], which leads to the two distinct combustion regions. Furthermore, as the CG mixing ratio increased, the content of carbon structure in the co-pyrolytic char decreased significantly, while the relative content of aliphatic rings and oxygen-containing functional groups decreased more markedly than that of aromatic rings, as evidenced by the results of XRD, Raman and FTIR. This phenomenon results in the both combustion zones moving towards the higher temperature, and the area of the low-temperature combustion zone corresponding to aliphatic rings and oxygen-containing functional groups shows a gradual decrease, while the area of the high-temperature combustion zone corresponding to aromatic rings exhibits a gradual increase shows a gradual increase. It should be noted that the increase in ash content impedes the contact between the gas and the active/available site, thereby reducing the combustion rate.

Meanwhile, the combustion parameters, including the initial temperature (T_i) and burnout temperature (T_f) were defined to evaluate the combustion parameters of the co-pyrolytic char samples[42]. The results are presented in Table 4, which demonstrates that the T_i value increases gradually with an increasing in the CG mixing ratio: 459.15 K (RS char) → 512.15 K (80RS20CG) → 536.15 K (60RS40CG) → 547.15 K (40RS60CG) → 552.15 K (20RS80CG) → 632.15 K (CG char). This suggests that the ignition temperature of the co-pyrolytic char increases with an increasing in the CG mixing ratio. A similar trend is observed in the burnout temperature, indicating that the co-pyrolytic char with a higher CG mixing ratio requires a higher temperature and longer time to burn out.

In addition, S and R_w related to ignition temperature, combustion rate, and burnout temperature were introduced to quantify the combustion reactivity and combustion stability of the char samples[22,43]. It should be noted that the larger S indicates the higher combustion reactivity, and the larger R_w means the more stable combustion, and the S and R_w can be described as[43,44]:

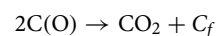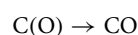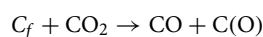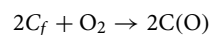| Sample	T_i (K)	T_{m-1} (K)	T_{m-2} (K)	T_f (K)	R_{max-1} (min^{-1})	R_{max-2} (min^{-1})
RS char	459.15	640.15	708.15	766.15	0.15	0.0294
80RS20CG	512.15	643.15	723.15	792.15	0.126	0.0306
60RS40CG	536.15	645.15	740.15	797.15	0.084	0.0528
40RS60CG	547.15	680.15	756.15	836.15	0.06	0.066
20RS80CG	552.15	729.15	765.15	853.15	0.084	0.072
CG char	632.15	–	771.15	912.15	-	0.132

Table 4. Combustion characteristic parameters of the char samples.

$$S = \frac{(dx/dt)_{\max} \times (dx/dt)_{mean}}{T_i^2 \times T_f} \tag{10}$$

$$R_w = \frac{560}{T_i} + \frac{650}{T_{\max}} + 0.27 \times (dx/dt)_{\max} \tag{11}$$

where $(dx/dt)_{max}$ is *the* maximum reaction rate of the sample, %/s, $(dx/dt)_{mean}$ is the average reaction rate of the char samples, $\min^{-1}$, and $T_{\max}$ is the temperature corresponding to the maximum reaction rate, K, respectively. The calculated values of S and R_w are shown in Fig. 10, and the results shows that values of S and R_w decrease as the CG mixing ratio increased, which indicates that an increase in the CG mixing ratio is associated with a reduction in the combustion reactivity of the co-pyrolytic samples and an increase in the instability of the combustion process.

As known, the char combustion process involves a sequence of adsorption and desorption processes, which can be expressed as follows[45]:

$$2C_f + O_2 \rightarrow 2C(O)$$

$$C_f + CO_2 \rightarrow CO + C(O)$$

$$C(O) \rightarrow CO$$

$$C(O) + O_2 \rightarrow CO_2/CO + C(O)$$

$$2C(O) \rightarrow CO_2 + C_f$$

where C_f and C(O) are referred to an active/available site and a carbon–oxygen complex, respectively. The char combustibility is contingent upon its surface-active sites and porous structure. The pore structure and SEM results have demonstrated that the pore structure undergoes a fluctuating trend as the CG mixing ratio increases. The formation of large pores facilitates the contact between gas and active/available sites, which is conducive to combustion. This indicates that the change in pore structure has a minimal impact on the combustibility of the co-pyrolytic char. The results of XRD, FTIR and Raman Spectroscopy have demonstrated that the contents of oxygen-containing and aliphatic groups in the co-pyrolytic char samples decreased with the increase of the CG mixing ratio, whereas the contents of aromatic groups exhibited an inverse trend. Furthermore, the combustibility of oxygen-containing and aliphatic groups was found to be higher than that of aromatic groups[4]. This suggests that the reduction in the combustibility of the co-pyrolytic char samples with the increasing CG mixing ratio is primarily influenced by the chemical structure. Furthermore, CG will introduce quartz and mullite to react with the alkali metal in RS to form aluminosilicate (shown in Fig. 8), which will result in the alkali metal losing its catalytic activity, thereby reducing the combustibility of the co-pyrolytic char.

In order to further quantify the effect of the CG mixing ratio on the combustibility of the co-pyrolytic char, the kinetics of RS char and 80RS20CG were analyzed by the Kissinger–Akahira–Sunose (KAS) method[46], and the equation was given as follow:
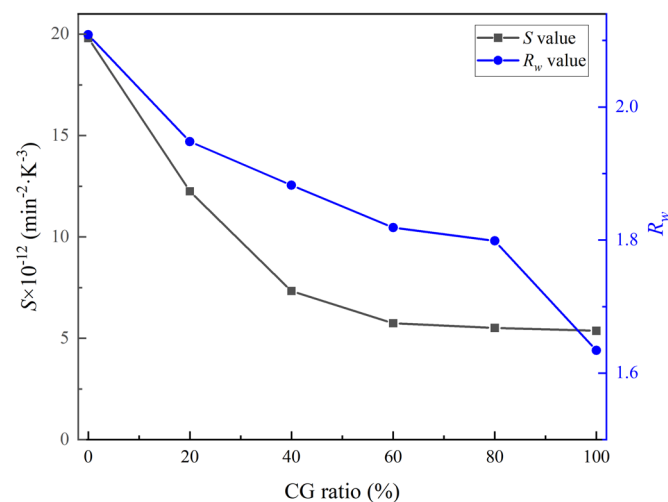

Figure 10. The calculated values of S and R_w of the co-pyrolytic char samples.

$$\ln\left(\frac{\beta}{T^2}\right) = \ln\left(\frac{k_0 R}{EG(x)}\right) - \frac{E}{RT} \tag{12}$$

where $G(x)$ is the reaction mechanism function; k_0 is the pre-exponential factor, min⁻¹; β is the heating rate, K/min; T is the absolute temperature, K; E is the activation energy, kJ/mol; R is the gas constant (8.314 J/(mol·K)).

The curves of the combustion conversion rate and reaction rate for the RS char and 80RS20CG at different heating ratios under the air atmosphere are shown in Figs. 11, and 12. The results show that the combustion conversion rate curves shift to a higher temperature region as the heating rate increases, due to the time lag caused by the heat transfer at a higher heating rate, and the temperature rises to the higher level before the combustion has progressed sufficiently, resulting in a higher temperature range for char to undergo mass loss. In contrast, at a lower heating rate, the temperature distribution in the char particles becomes more homogeneous, resulting in more adequate combustion and less mass loss of the co-pyrolytic char sample.

Whereas the KAS model adheres to a linear functional form ($Y = kX + b$) and the E could be determined by the calculated slope of the line plotting the left side of the equation against $-1/T$ for a given degree of conversion. In addition, the combustion of the co-pyrolytic char is generally considered to be a first order reaction, so the reaction mechanism can be described as $G(x) = -\ln(1-x)$[45,47]. Thus, the values of k_0 can be calculated from the intercept of the fitted lines. The fitting curves are shown in Fig. 13, and the kinetic equations, values of E, k_0 and correlation coefficients (R^2) at different combustion conversion rates are presented in Table 5. As shown in Fig. 13 and Table 5, the correlation coefficients (R^2) for each equation are consistently above 0.95, providing substantial confidence in the calculations and data reliability. The calculated E values of RS char at different conversion rates are in the range of 89.87–144.67 kJ/mol, which are lower than that of 80RS20CG (102.22–164.99 kJ/mol).

The structural characterization of co-pyrolytic char samples with varying mixing ratios of RS and CG demonstrate that the mixing ratio exerts a significant influence on the physicochemical properties of co-pyrolytic
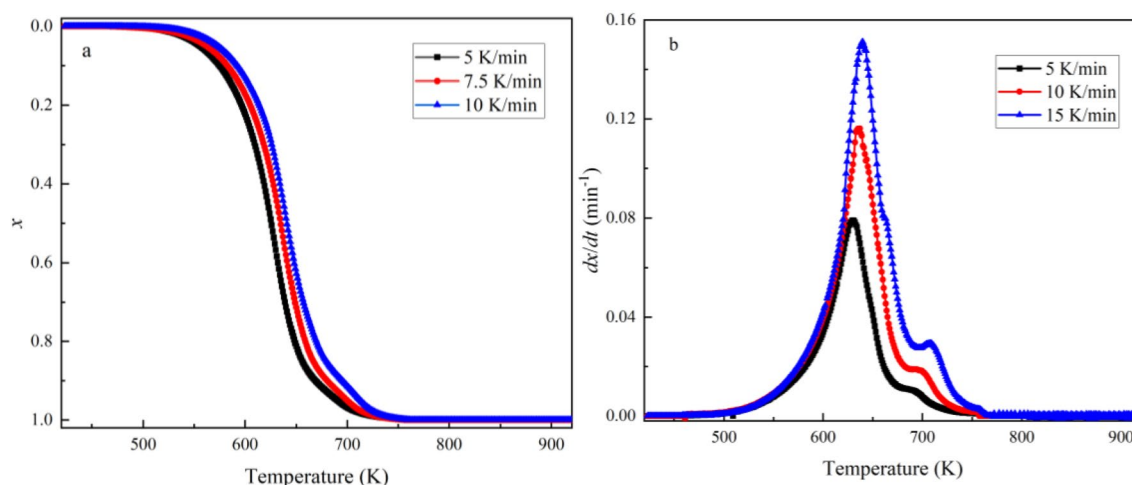

Figure 11. Combustion conversion rate (x) and reaction rate (dx/dt) curves of the RS char at different heating rates.
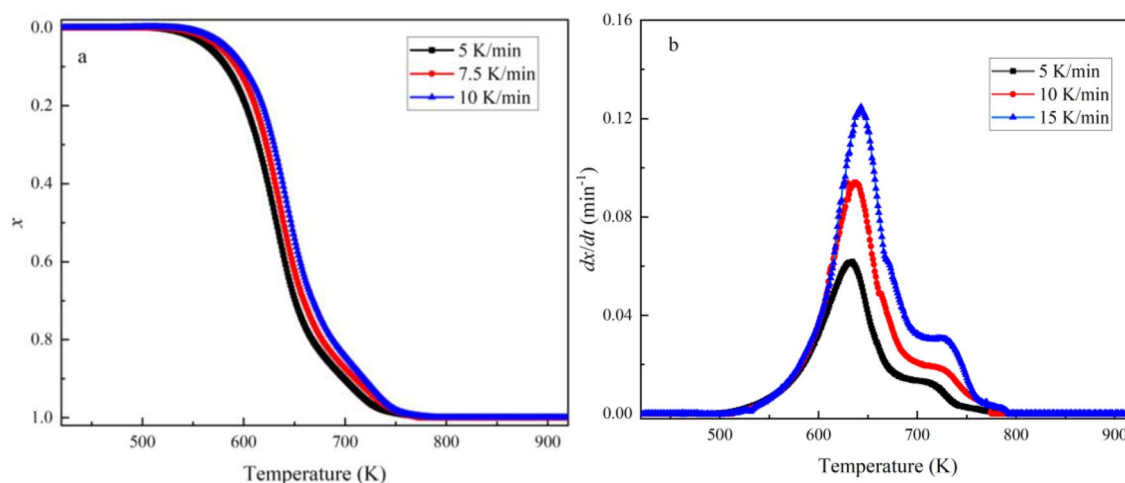

Figure 12. Combustion conversion rate (x) and reaction rate (dx/dt) curves of the 80RS20CG at different heating rates.
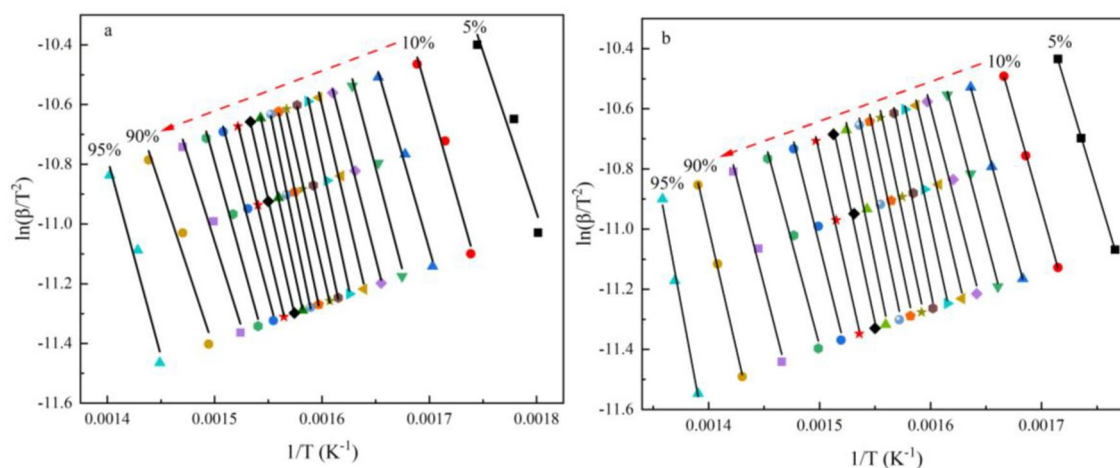
Figure 13. Kinetic fitting curves of the combustion conversion rate (**a**. RS char, **b**. 80RS20CG).

char samples, including their morphology, organic functional groups, and inorganic minerals. An increase in the CG mixing ratio will result in an increase in the aromatic, accompanied by a reduction in the content of aliphatic hydrocarbons and oxygen-containing groups. The presence of mullite and quartz in the CG will result in the formation of stable aluminosilicates when in contact with alkali metals in the RS, lead to the loss of the catalytic effect of alkali metals on the subsequent combustion of the co-pyrolytic char. While the pore structure shows an initial increase and subsequent decrease as the CG mixing ratio increased. The results of the combustion characteristics analysis indicate that the combustibility of the co-pyrolytic char decreases with an increase in the CG mixing ratio. The experimental findings and results presented above indicate that the aromatization of the carbon structure is a significant factor contributing to the reduced combustibility of the co-pyrolytic char.

A collaborative approach utilizing XRD, Raman, FTIR and TGA has systematically presented the influence of the mixing ratio on the evolution of the physicochemical properties as well as the combustibility of the co-pyrolytic char. This helps to elucidate the influence of the mixing ratio on the co-combustion behavior of RS and CG in a more comprehensive manner.

Conclusion

The physicochemical properties and combustion characteristics of the co-pyrolytic char prepared under a N_2 atmosphere with different mixing ratios of RS and CG were investigated in this study. The main conclusions are summarized as follows.

1. The introduction of CG will increase the ignition and burnout temperature, as well as prolong the co-pyrolytic char combustion time.
2. The deterioration in the combustibility of co-pyrolytic char with an increase in the CG mixing ratio can be attributed to the increase in the content of aromatic and the decrease in the content of aliphatic hydrocarbons and oxygen-containing groups.
3. The mullite and quartz in the CG will react with alkali metals in the RS to form aluminosilicate, which reduces the catalytic ability of alkali metals for the co-pyrolytic char combustion.
4. The combustion kinetics of RS char and 80RS20CG were analyzed by the KAS method, and the activation energy of the 80RS20CG is 102.22–164.99 kJ/mol, which is higher than 89.87–144.67 kJ/mol of RS char.

Future studies will extend to the investigation of feedstock types and operating conditions, including temperature and pressure, as well as pollutant emissions during the co-combustion of RS and CG.

Samples	x	Kinetic equation	E (kJ/mol)	k_0 (min^{-1})	R^2
RS char	0.05	y = −10,809.82X + 8.49	89.87	2.63E+04	0.95
	0.10	y = −12,675.23X + 10.96	105.38	7.30E+05	0.98
	0.15	y = −12,501.07X + 10.17	103.93	4.90E+05	0.99
	0.20	y = −13,693.99X + 11.78	113.85	3.58E+06	0.98
	0.25	y = −14,111.97X + 12.17	117.33	6.81E+06	0.99
	0.30	y = −15,325.94X + 13.92	127.42	5.11E+07	0.99
	0.35	y = −16,710.41X + 15.94	138.93	4.90E+08	0.99
	0.40	y = −16,838.52X + 15.95	139.99	5.70E+08	0.99
	0.45	y = −15,805.32X + 14.14	131.41	9.86E+07	0.99
	0.50	y = −17,231.20X + 16.24	143.26	9.76E+08	0.99
	0.55	y = −17,400.88X + 16.37	144.67	1.23E+09	0.99
	0.60	y = −16,496.65X + 14.81	137.15	2.68E+08	0.99
	0.65	y = −15,581.89X + 13.23	129.55	5.66E+07	0.99
	0.70	y = −14,908.54X + 12.02	123.95	1.74E+07	0.99
	0.75	y = −13,487.15X + 9.66	112.13	1.59E+06	0.99
	0.80	y = −13,009.17X + 8.72	108.16	6.40E+05	0.98
	0.85	y = −11,486.69X + 6.17	95.50	4.69E+04	0.98
	0.90	y = −10,866.92X + 4.88	90.35	1.29E+04	0.96
	0.95	y = −13,269.38X + 7.80	110.32	3.09E+05	0.97
80RS20CG	0.05	y = −12,295.26X + 10.65	102.22	2.66E+07	0.99
	0.10	y = −13,068.73X + 11.28	108.65	1.09E+08	0.99
	0.15	y = −13,582.1X + 11.69	112.92	2.63E+08	0.99
	0.20	y = −14,015.76X + 12.10	116.53	5.63E+08	0.99
	0.25	y = −14,266.01X + 12.23	118.61	8.41E+08	0.96
	0.30	y = −15,532.96X + 14.08	129.14	7.22E+09	0.98
	0.35	y = −16,934.11X + 16.11	140.79	7.24E+10	0.99
	0.40	y = −18,469.68X + 18.35	153.56	8.79E+11	0.98
	0.45	y = −17,320.53X + 16.33	144.00	1.28E+11	0.96
	0.50	y = −17,547.18X + 16.50	145.89	1.78E+11	0.96
	0.55	y = −17,775.08X + 16.67	147.78	2.46E+11	0.96
	0.60	y = −18,062.66X + 16.88	150.17	3.55E+11	0.96
	0.65	y = −17,184.25X + 15.32	142.87	8.12E+10	0.98
	0.70	y = −16,461.94X + 13.94	136.86	2.24E+10	0.99
	0.75	y = −14,880.22X + 11.26	123.71	1.60E+09	0.97
	0.80	y = −13,765.71X + 9.26	114.45	2.33E+08	0.97
	0.85	y = −14,412.22X + 9.71	119.82	4.51E+08	0.97
	0.90	y = −16,044.56X + 11.46	133.39	3.50E+09	1.00
	0.95	y = −19,844.85X + 16.04	164.99	5.50E+11	0.99

Table 5. Kinetic parameters of RS char and 80RS20CG at different combustion conversion rate.

Data availability

The datasets used and/or analyzed during the current study available from the corresponding author on reasonable request.

References

1. Cao, L. *et al.* Biorenewable hydrogen production through biomass gasification: A review and future prospects. *Environ. Res.* **186**, 109547–109559 (2020).
2. Awasthi, M. K. *et al.* A comprehensive review on thermochemical, and biochemical conversion methods of lignocellulosic biomass into valuable end product. *Fuel* **342**, 127790–127798 (2023).
3. Cortazar, M. *et al.* A comprehensive review of primary strategies for tar removal in biomass gasification. *Energy Convers. Manag.* **276**, 116496–116531 (2023).
4. Wang, G. *et al.* Hydrothermal carbonization of maize straw for hydrochar production and its injection for blast furnace. *Appl. Energy* **266**, 114818–114829 (2020).
5. Sousa, M. H., Silva, A. S. F., Correia, R. C. & Leite, N. P. Valorizing municipal organic waste to produce biodiesel, biogas, organic fertilizer, and value-added chemicals: An integrated biorefinery approach. *Biomass Convers. Biorefinery* **12**, 1–15 (2022).

6. Aqsha, A., Tijani, M. M., Moghtaderi, B. & Mahinpey, N. Catalytic pyrolysis of straw biomasses (wheat, flax, oat and barley) and the comparison of their product yields. *J. Anal. Appl. Pyrol.* **125**, 201–208 (2017).
7. Wu, Y. *et al.* Applications of catalysts in thermochemical conversion of biomass (pyrolysis, hydrothermal liquefaction and gasification): A critical review. *Renew. Energy* **196**, 462–481 (2022).
8. Jayaraman, K., Kok, M. V. & Gokalp, I. Combustion properties and kinetics of different biomass samples using TG-MS technique. *J. Therm. Anal. Calorim.* **127**, 1361–1370 (2017).
9. Yanqing, N., Houzhang, T. & Shi'En, H. Ash-related issues during biomass combustion: Alkali-induced slagging, silicate melt-induced slagging (ash fusion), agglomeration, corrosion, ash utilization, and related countermeasures. *Prog. Energy Combust. Sci.* **52**, 1–61 (2016).
10. Garba, M. U. *et al.* Prediction of potassium chloride sulfation and its effect on deposition in biomass-fired boilers. *Energy Fuels* **26**, 6501–6508 (2012).
11. Chartrand, B. P. Towards a comprehensive thermodynamic database for ash-forming elements in biomass and waste combustion: Current situation and future developments. *Fuel Process. Technol.* **105**, 129–141 (2013).
12. Zhang, H. *et al.* Preheating pyrolysis-char combustion characteristics and kinetic analysis of ultra-low calorific value coal gangue: Thermogravimetric study. *Appl. Therm. Eng.* **229**, 120583–120591 (2023).
13. Liu, L. *et al.* Experimental study on K migration, ash fouling/slagging behaviors and CO_2 emission during co-combustion of rice straw and coal gangue. *Energy* **251**, 123950–123958 (2022).
14. Wu, W. *et al.* Combustion ash addition promotes the production of K-enriched biochar and K release characteristics. *J. Clean. Prod.* **311**, 127557–127565 (2021).
15. Gai, D. *et al.* Catalytic performance and mechanism of A-site vacancy deficient perovskite catalyst over tar cracking during biomass pyrolysis. *J. Clean. Prod.* **405**, 136876–136885 (2023).
16. Zhang, Y. *et al.* Air and oxy-fuel combustion characteristics of coal gangue and weathered coal blends. *Energy* **284**, 128660–128667 (2023).
17. Bi, H. *et al.* Influence of biomass on multi-component reaction model and combustion products of coal gangue. *Combust. Flame* **240**, 111999–112013 (2022).
18. Zhang, Y., Zhao, J., Ma, Z., Yang, F. & Cheng, F. Effect of oxygen concentration on oxy-fuel combustion characteristic and interactions of coal gangue and pine sawdust. *Waste Manag.* **87**, 288–294 (2019).
19. Bi, H. *et al.* Combustion behavior, kinetics, gas emission characteristics and artificial neural network modeling of coal gangue and biomass via TG-FTIR. *Energy* **213**, 118790–118802 (2020).
20. Li, J., Hu, X. & Qiao, X. Thermogravimetric experimental study on the co-combustion of coal gangue and polypropylene. *Thermochim. Acta* **732**, 179660–179669 (2024).
21. Zhou, C., Liu, G., Xu, Z., Sun, H. & Lam, P. K. S. The retention mechanism, transformation behavior and environmental implication of trace element during co-combustion coal gangue with soybean stalk. *Fuel* **189**, 32–38 (2017).
22. Gong, Z., Song, C., Li, Y. & Li, Z. Combustion characteristics of coal gangue and biomass under an O_2/CO_2 atmosphere. *Therm. Sci.* **24**, 61–61 (2020).
23. Zhou, C., Liu, G., Cheng, S., Fang, T. & Lam, P. K. S. Thermochemical and trace element behavior of coal gangue, agricultural biomass and their blends during co-combustion. *Bioresour. Technol.* **166**, 243–251 (2014).
24. Zhou, C., Liu, G., Fang, T. & Lam, P. Investigation on thermal and trace element characteristics during co-combustion biomass with coal gangue. *Bioresour. Technol.* **175**, 454–462 (2015).
25. Tian, B. *et al.* Understanding the pyrolysis synergy of biomass and coal blends based on volatile release, kinetics and char structure. *Biomass Bioenergy* **168**, 106687–106697 (2023).
26. Zou, X. *et al.* In-depth understanding of the microscopic mechanism of biochar carbonaceous structures during thermochemical conversion: Pyrolysis, combustion and gasification. *Fuel* **361**, 106687–106703 (2024).
27. Tilghman, M. B. & Mitchell, R. E. Coal and biomass char reactivities in gasification and combustion environments. *Combust. Flame* **162**, 3220–3235 (2015).
28. Tong, W. *et al.* Effect of pore structure on CO_2 gasification reactivity of biomass chars under high-temperature pyrolysis. *J. Energy Inst.* **93**, 962–976 (2020).
29. Zeineb, B. *et al.* Thermogravimetric study on the influence of structural, textural and chemical properties of biomass chars on CO_2 gasification reactivity. *Energy* **88**, 703–710 (2015).
30. Huo, X. *et al.* Investigation of co-pyrolysis characteristics of modified coal gangue and biomass. *Thermochim. Acta* **705**, 179033–179036 (2021).
31. Cha, J. S. *et al.* Production and utilization of biochar: A review. *J. Ind Eng. Chem.* **40**, 1–15 (2016).
32. Bi, H. *et al.* Pyrolysis characteristics, artificial neural network modeling and environmental impact of coal gangue and biomass by TG-FTIR. *Sci. Total Environ.* **751**, 142293–142304 (2021).
33. Giudicianni, P., Cardone, G. & Ragucci, R. Cellulose, hemicellulose and lignin slow steam pyrolysis: Thermal decomposition of biomass components mixtures. *J. Anal. Appl. Pyrol.* **100**, 213–222 (2013).
34. Yang, H., Yan, R., Chen, H., Zheng, C. & Liang, D. T. In-depth investigation of biomass pyrolysis based on three major components: Hemicellulose, cellulose and lignin. *Energy Fuels* **20**, 388–393 (2011).
35. Liu, L., Cao, Y. & Liu, Q. Kinetics studies and structure characteristics of coal char under pressurized CO_2 gasification conditions. *Fuel* **146**, 103–110 (2015).
36. Jiang, M.-Q., Zhou, R., Hu, J., Wang, F.-C. & Wang, J. Calcium-promoted catalytic activity of potassium carbonate for steam gasification of coal char: Influences of calcium species. *Fuel* **99**, 64–71 (2012).
37. Liu, L., Kong, B., Yang, J., Liu, Q. & Liu, X. CO_2 gasification kinetics and structural characteristics of tri-high coal char prepared at elevated temperature. *ACS Omega* **5**, 507–517 (2020).
38. Niu, Y., Hu, Y. & Wang, W. Co-gasification of coal gangue and pine sawdust on a self-made two-stage fixed bed: Effect of mixing ratio. *Int. J. Hydrog. Energy* **47**, 21713–21724 (2022).
39. Lin, B., Zhou, J., Qin, Q., Xie, C. & Luo, Z. Physicochemical characteristics of biomass- coal blend char: The role of co- pyrolysis synergy. *Energy Sci. Eng.* **9**, 1249–1262 (2021).
40. Sonibare, O. O., Haeger, T. & Foley, S. F. Structural characterization of Nigerian coals by X-ray diffraction, Raman and FTIR spectroscopy. *Energy* **35**, 5347–5353 (2010).
41. Fu, P., Yi, W., Li, Z., Bai, X. & Wang, L. Evolution of char structural features during fast pyrolysis of corn straw with solid heat carriers in a novel V-shaped down tube reactor. *Energy Convers. Manag.* **149**, 570–578 (2017).
42. Xu, Y. *et al.* Experimental study on the comprehensive behavior of combustion for blended coals. *Asia Pac. J. Chem. Eng.* **5**, 435–440 (2010).
43. Chen, X., Zhang, Y., Zhang, Q., Li, C. & Zhou, Q. Thermal analyses of the lignite combustion in oxygen-enriched atmosphere. *Therm. Sci.* **19**, 801–811 (2015).
44. Huang, X., Jiang, X., Han, X. & Wang, H. Combustion characteristics Of fine- and micro-pulverized coal in the mixture Of O_2/CO_2. *Energy Fuels* **22**, 3756–3762 (2008).
45. Tong, W. *et al.* Experiment and expectation: Co-combustion behavior of anthracite and biomass char. *Bioresour. Technol.* **280**, 412–420 (2019).
46. He, K. Reaction kinetics in differential thermal analysis. *Anal. Chem.* **29**, 1417–1421 (1957).

47. Ullah, H. *et al.* Combustion characteristics and retention-emission of selenium during co-firing of torrefied biomass and its blends with high ash coal. *Bioresour. Technol.* **245**, 73–80 (2017).

Acknowledgements

Author contributions

C.X.: Conceptualization, Methodology, original draft preparation, Formal analysis, Investigation. C.L.: Writing-Reviewing, Investigation; J.D.: Writing-Reviewing, Investigation; L.L.: Conceptualization, Methodology, Investigation, Writing-Reviewing & Editing, Funding acquisition, Supervision; J.W.: Investigation; C.Y.: Investigation; J.G.: Investigation.

Competing interests

The authors declare no competing interests.

Additional information

Correspondence and requests for materials should be addressed to L.L.

Reprints and permissions information is available at www.nature.com/reprints.

Publisher's note Springer Nature remains neutral with regard to jurisdictional claims in published maps and institutional affiliations.